Medium-Fidelity CFD Modeling of Multicopter Wakes for Airborne Sensor Measurements

Jonathan Chiew
Research Aerospace Engineer
NASA Ames Research Center
Moffett Field, CA, USA

Michael Aftosmis
Aerospace Engineer
NASA Ames Research Center
Moffett Field, CA, USA

Kristen Manies
Ecologist
US Geological Survey
Menlo Park, CA, USA

ABSTRACT

A steady-state multicopter simulation capability leveraging automated Cartesian grid generation and a blade element source term rotor model was used to investigate multi-rotor aerodynamics in and out of ground effect. Simulations demonstrated that this model is able to predict reasonably accurate thrust in ground effect for both single and multiple propeller cases. The method yielded accurate lift and drag predictions for a commercial quadcopter when compared to recent wind tunnel test data. This aircraft was then simulated in a variety of flight conditions, including both hover and edgewise forward flight, to determine if generalized guidelines for airborne sensor placement could be developed. Velocity perturbation magnitudes showed large regions of affected air upstream of the vehicle at low speeds, which contracted as the vehicle's speed was increased. Placing the sensors more than one characteristic length ahead of or above the aircraft reduces errors from rotor-induced flow at higher speeds. For low-speed forward flight, the entrainment of flow into the propeller wakes introduces significant flow turning above the aircraft, suggesting that a forward location, with more moderate perturbations, could be advantageous for these conditions.

NOTATION

English

sUAS	Small uncrewed aircraft system(s)
CFD	Computational Fluid Dynamics
DJI	Da-Jiang Innovations
IGE	In ground effect
OGE	Out of ground effect
RPM	Revolutions per minute (1/min)
N_b	Number of blades
R	Propeller radius
$\mathbf{v}$	Velocity vector
v_∞	Freestream velocity
z	Height above ground
T	Thrust, force parallel to propeller axis (lbs)
C_T	Thrust coefficient, $T/\rho A\left(\Omega R\right)^2$
s_d	Distance between propeller rotation axes
p	Static pressure
p_0	Stagnation pressure, $p+\frac{1}{2}\rho\left\|\mathbf{v}\right\|^2$

Greek

Ω	Rotational velocity (rad/sec)
μ	Advance Ratio, $v_\infty/\Omega R$
ρ	Density

Subscript

∞	Freestream or far-field value

Presented at the Vertical Flight Society's 78th Annual Forum & Technology Display, Ft. Worth, Texas, USA, May 10–12, 2022.

INTRODUCTION

Recent advances in battery and controls technology have led to the development of a variety of low-cost, remotely-piloted aircraft known as small uncrewed aircraft systems, or sUAS. One common use of sUAS is as an aerial platform for scientific measurements. Multi-rotor aircraft are commonly employed for these missions because of their hovering capability and low speed maneuverability. However, the interactional aerodynamics of multiple propellers raises questions about sensor placement in order to minimize error and uncertainty in the desired measurements.

Various studies have come to different conclusions as to the best location for wind and gas/particulate sensors such that effects from the propellers are minimized. Researchers have placed these instruments in various positions: below the aircraft fuselage, on a mast above the propellers, or on a boom extending in front of the vehicle (Refs. 1–4).

The growing interest in sUAS across academia, government, and industry has sparked significant computational and experimental research in the aerodynamics of these aircraft. Throneberry et al. (Ref. 5) provide an excellent review of recent work in this area as well as a discussion of recommendations for further research. One particular area of recent research is ground, ceiling, and wall effects for multi-rotor aircraft. Matus-Vargas et al. detail much of the recent research on this topic in their review paper (Ref. 6).

The present work focuses on two main areas: multi-rotor ground effect aerodynamics and the near-body flow-field of multicopters towards developing airborne sensor placement guidelines. Ground effect is an excellent starting place as it is more general than flight with ceiling and wall effects, since

nearly all aircraft take-off from and land on the ground. This work provides validation of a medium-fidelity CFD model for predicting multi-rotor ground effect aerodynamics in hovering flight and explores some of the differences between published experimental and computational results for quadrotors. It also examines the accuracy of an experimentally derived model for multi-rotor ground effect thrust augmentation (Ref. 7). In the second section, simulations of a DJI Phantom 3 are performed to assess the merits of various airborne sensor placement locations and their sensitivity to several vehicle parameters.

TECHNICAL APPROACH

This work employs a widely-used simulation framework that solves the three dimensional inviscid flow equations on a multilevel Cartesian mesh with embedded boundaries is employed in this work (Ref. 8). The mesh consists of regular Cartesian hexahedra everywhere, except for a layer of "cut cells" adjacent to the body of interest, which are arbitrarily-shaped polyhedra (Ref. 9). The spatial discretization employs a cell-centered, second-order accurate finite volume method with a weak imposition of both far-field and surface boundary conditions. Consistent with a medium-fidelity approach, all simulations in this work are steady state, although both first- and second-order accurate implicit backward difference time integration methods are available for unsteady simulations. The governing flow equations are closed with the ideal gas equation of state and solved using a non-linear multigrid method and Runge-Kutta smoothing.

For the steady-state solutions, the propeller effects are modeled with volumetric momentum and energy source terms in the governing equations (Refs. 10, 11). In each cell of the computational mesh, the propeller source terms are computed by first interrogating the computational flow-field to determine a local angle of attack and Mach number. With these in hand, aerodynamic lift and drag forces can then be computed by interpolating tabulated airfoil performance data. In this work, the airfoil tables blend both analytic (thin airfoil theory) and two-dimensional computational results to encompass the full range of angles of attack from -180° to 180° while providing more accurate lift and drag coefficients near the nominal operating conditions (Ref. 12). Airfoil ordinates were taken from laser scan data (Ref. 13) from over 20 different radial cuts through the propeller, although non-destructive methods such as photogrammetry can be a reasonable alternative (Ref. 14).

SINGLE PROPELLER VALIDATION

The present model has been previously validated for both large (Ref. 15) and small rotors (Ref. 12), but recent simulations of the DJI Phantom 3 aircraft have focused on time-accurate simulations (Ref. 11). Therefore, this section begins with a brief discussion of the steady-state rotor model as it relates to the previously published results and then continues with a validation of this method for the DJI Phantom 3 propeller in OGE hover. After presenting the results of this validation effort, an isolated propeller ground effect study is performed to demonstrate the ability of the method to capture ground effect thrust augmentation at constant RPM.

Steady-state Propeller Model

The integral velocity sampling unsteady rotor model previously published permitted arbitrarily large timesteps to be taken (Ref. 10). One straightforward approach to a steady state rotor model would simply take a timestep equivalent to $\frac{1}{N_b}$ propeller revolution. However, when using integral velocity sampling to determine local flow conditions, the spatial and temporal resolutions are directly coupled and the computed angle of attack would be averaged around the entire azimuth at each radial station. This is a reasonable approximation for an isolated propeller in hover, but is generally invalid, especial when considering an installed propeller or during edgewise forward flight. Cell local angle of attack and Mach number sampling has been routinely used for steady-state simulations with excellent results. In the context of integral sampling, this can be interpreted as ensemble averaging on a cylindrical mesh where the grid lines align with the blade position. On a Cartesian mesh the grid lines are not azimuthally aligned, however this is still a reasonable approximation as will be shown in the following section.

Hover Validation

Validation of this simulation approach begins with an isolated DJI Phantom 3 propeller in hovering flight out of ground effect. The farfield boundaries are placed 60 propeller radii away and are formulated using characteristics based on Riemann invariants. The lower boundary employs a slip wall formulation (inviscid ground plane) and is located 20 radii beneath the propeller center, well out of ground effect. A sequence of computational meshes is created using feature-based adaptation. The first mesh (37K cells) has a pre-specified refinement box containing the propeller source region. Each subsequent mesh reduces the finest cell spacing by a factor of 2 and targets adaptation in regions with large undivided first differences of velocity magnitude. Figure 1 demonstrates excellent grid convergence of thrust coefficient on these adapted meshes. Cell spacing is normalized by tip chord, and the propeller's rotational velocity is 4000 RPM. The second finest mesh contains about 8 million cells after 3 adaptation cycles and is used for the hover validation effort. Each case ran in about 2 hours using 140 Cascade Lake cores on the NASA Endeavour supercomputer.

Having demonstrated mesh convergence of the modeling approach using local flow-field sampling, the propeller speed was varied from 3000 to 7500 RPM and compared to the NASA Ames multicopter test data (Ref. 13). Figure 2 is a plot of the propeller's torque required versus thrust. The CFD predictions match the experimental data well across the range of propeller RPM. There is a very slight difference in slope, which could result from modeling errors in the blade element

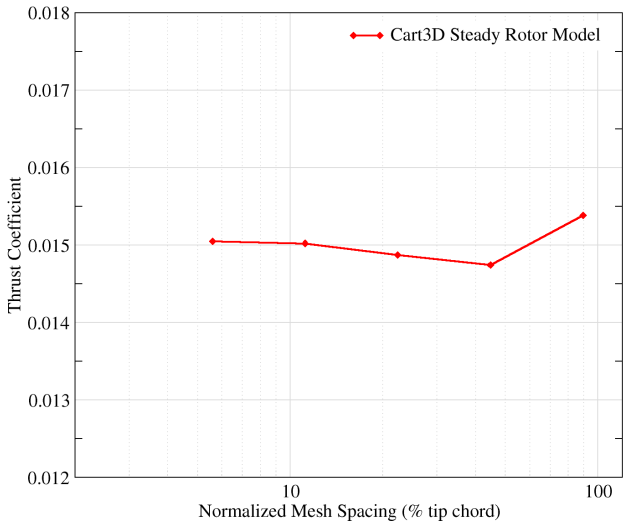

Figure 1. Excellent grid convergence of the velocity magnitude adapted meshes for a DJI Phantom 3 isolated propeller hovering out of ground effect (4000 RPM).

assumptions, computed airfoil tables, or inviscid wake modeling, but overall the correlation is very good and well within the experimental uncertainty.

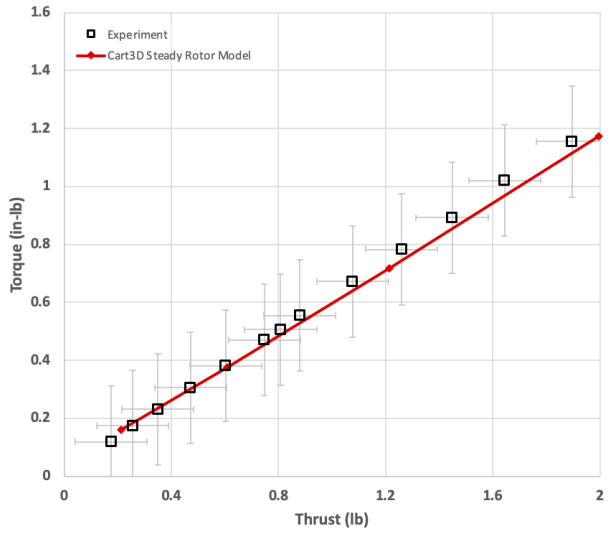

Figure 2. Thrust vs. torque for DJI Phantom 3 isolated propeller in hover (OGE) at various RPM. The Cart3D steady rotor model closely matches the data (Ref. 13) to well within the experimental uncertainty.

Hovering Flight in Ground Effect

Ground effect aerodynamics for single main rotor helicopters has been well studied both analytically and experimentally. Cheeseman and Bennett developed a model for predicting IGE thrust augmentation for both hovering and forward flight (Ref. 16). Their model used momentum theory and the method of images, assuming uniform inflow and induced velocity (from the image rotor) over the disk. In this present work, only the limiting case of zero forward speed is considered, which results in the well-known classical IGE thrust model for hover:

$$\frac{T_{IGE}}{T_{OGE}} = \frac{1}{1-\left(\frac{R}{4z}\right)^2} \tag{1}$$

This model compares well to experimental data for large rotors (Ref. 17) and has been recently investigated for small, low Reynolds number propellers typically used on sUAS. The experimental studies show that the model remains an excellent approximation for single propeller thrust in ground effect (Refs. 7, 18). The computational study of Paz et al. (Ref. 19) showed reasonable correlation with the Cheeseman-Bennett model as well, although some differences were found when the steady-state multiple reference frame approach was compared to the time-accurate sliding mesh model.

A series of hover simulations at various heights above ground was performed to develop confidence in the steady medium-fidelity approach which models propellers with source terms and the ground plane using an inviscid wall. The feature-based mesh adaptation from the OGE hover simulations is used for the IGE simulations. Figure 3 shows the variation of non-dimensional thrust with height above ground. The CFD predicted ground effect thrust variation (labeled "Cart3D") is in excellent agreement with the theoretical model of Cheeseman-Bennett.

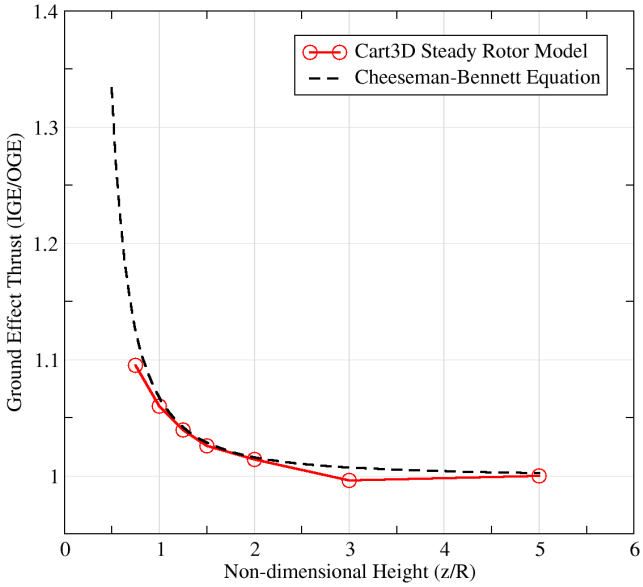

Figure 3. Thrust increase at different heights when hovering in ground effect for isolated DJI Phantom 3 propeller. Simulation results correlate well to the theoretical model of Cheeseman-Bennett.

MULTI-ROTOR AERODYNAMICS IN GROUND EFFECT

Multi-rotor ground effect aerodynamics has recently become a topic of interest with the emergence and widespread utilization of sUAS. Having developed confidence in the present

model for predicting a single propeller's thrust in ground effect at various heights above the ground, dual propeller systems are considered next before investigating quadruple propeller configurations. In each arrangement, the propellers are modeled identically and placed at the same height above the ground plane. Only the rotation directions are changed to minimize hover yaw moments as is typical for a multicopter in hover.

Two Propellers

The simple dual fixed-pitch propeller system considered here has limited utility for an aircraft due to the lack of sufficient control inputs; however, it serves as a useful building block before considering configurations with more propellers. Some researchers have suggested that multi-rotor ground effect models should be scaled to an equivalent radius based on the total area of all the rotors. There is some merit to this concept since the characteristic length scale of the flow may no longer be the radius of a single rotor, at least for closely packed cases. However, one would also expect a sensitivity to separation distance because if $s_d \gg R$, the characteristic length scale should be that of a single rotor. For a (non-overlapped) twin rotor system, this would shift the ground effect thrust curve by the factor $\sqrt{2}$.

Griffiths & Leishman (Ref. 20) analyzed a lateral twin rotor configuration in ground effect using a free-wake vortex method. For the rotor spacing considered ($1.25D$), they discovered an upwash between the two rotors similar to tiltrotor "fountain flow" recirculation above the fuselage between the wings. However, their study was performed at a constant thrust coefficient of 0.015 and did not report the power required at each height above ground. Recently, He (Ref. 21) investigated multi-rotor ground effect aerodynamics experimentally towards developing a novel IGE thrust model free of singularities, unlike the Cheeseman-Bennett model which is singular at $z/R = 0.25$. The dual-propeller experiments demonstrated a modest sensitivity to the separation distance between the propellers. Consistent with intuition, at very large separation distances, dual propeller thrust behaved similarly to an isolated propeller in ground effect. However, IGE thrust at close spacings ($s_d \approx R$) also reverted to the isolated propeller curve, while some differences were found at the intermediate distances. The IGE thrust augmentation was found to be generally insensitive to propeller rotation direction or velocity.

Figure 4 depicts the velocity field (colored by magnitude) around two DJI Phantom 3 propellers hovering in ground effect at a height of $z/R_{eq} = 1.25$ on the $y = 0$ cutting plane. The separation distance is identical to that of the production quadcopter ($s_d = 1.036R$), much closer than in the lateral twin proprotor study of Griffiths & Leishman. The flow-field does not show significant upward flow between the propellers, likely due to their close spacing. Otsuka et al. (Ref. 22) observed this phenomenon in their experimental wake visualizations, where they found a reduction in so-called "soaring flow" at the center of the quadcopter when the propellers were more tightly spaced.

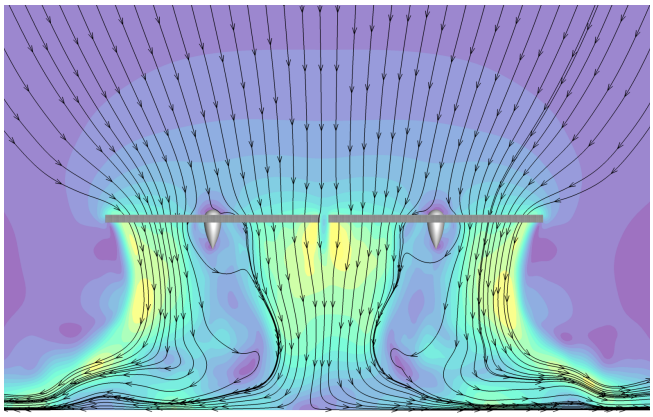

Figure 4. Velocity magnitude (yellow=high, blue=low) with surface streamlines on $y = 0$ cutting plane, showing little upwards flow between the closely-spaced propellers. Rotor hexes are shown in gray and axisymmetric centerbodies in light gray.

Figure 5 shows the thrust augmentation in ground effect for this twin propeller system. When rescaled to the equivalent radius, the model does not match the Cheeseman-Bennett model. In fact, the unscaled results match the model much more closely, which is consistent with He's experimental results for tightly spaced twin rotor configurations. Given the lack of "fountain flow" between the propellers in the simulation, this is a reasonable result. It is possible that the equivalent radius scaling may be valid for intermediate spacings, where He's data did show a difference between single and twin propeller systems, however, it is clear that the scaling is not valid in general.

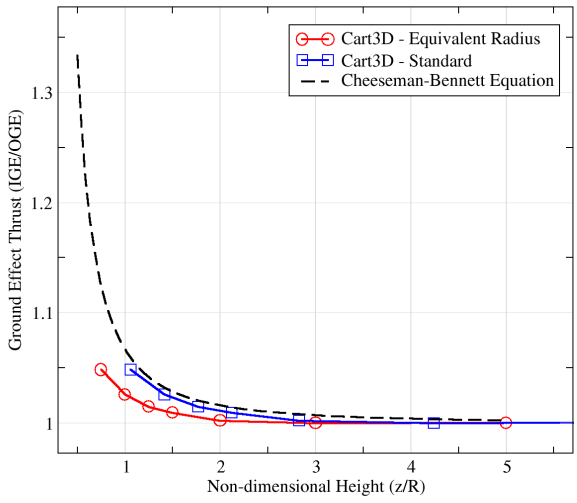

Figure 5. Twin propeller ($s_d = 1.036$) thrust in ground effect at various heights plotted as actual geometric height ("standard") and scaled to an equivalent-area radius. At this spacing, the twin propellers behave similarly to a single propeller in ground effect, as shown by the Cheeseman-Bennett model.

Four Propellers

Next, a simple quadruple propeller configuration is considered with diagonally opposed propellers spinning in the same direction. The separation distance is kept constant at $s_d = 1.036R$, and as a result, this configuration is essentially the DJI Phantom 3 aircraft without a fuselage. In this case, the equivalent-area radial scaling is found to produce better results than the curve based on actual height above ground (Figure 6). This is consistent with the literature that the classical (unscaled) Cheeseman-Bennett model (Equation 1) is not a good approximation for the thrust of a quadcopter hovering in ground effect. Sanchez-Cuevas et al. derived the extension of the Cheeseman-Bennett model for a quadcopter with four image sources below the ground plane (Ref. 23):

$$\frac{T_{IGE}}{T_{OGE}} = \frac{1}{1-\left(\frac{R}{4z}\right)^2 - \frac{zR^2}{\left(s_d^2+4z^2\right)^{3/2}} - \frac{0.5zR^2}{\left(2s_d^2+4z^2\right)^{3/2}}} \qquad (2)$$

The derivation of Equation 2 assumes a uniform distribution of induced velocity over each propeller disk and neglects the induced flow in the plane of the rotors. Nevertheless, Figure 6 shows that this model (green) is a reasonable model for this case. In their work, they found significant upload (vertical force) on the fuselage and accounted for this by adding another correction term to the model based on the induced velocity at point in the middle of the four propellers, with a coefficient tuned to their experimental results, which showed ground effects up to around $z/R = 5$. Note that in Conyers's curve fit ground effect thrust model, the propeller spacing coefficients would be extrapolated significantly beyond the tested range and would likely be invalid. Both the equivalent-area scaling and S-C-H-O model (Equation 2) provide reasonable estimates of ground effect thrust for this configuration, but further study is warranted to assess the generalizability of each model.

Figure 7 visualizes the velocity field for the quad propeller configuration on the $y = 0$ cutting plane at a $z/r_{eq} = 3$. There is some flow recirculation in between the four propellers as shown by the streamlines, but minimal "fountain flow" likely due to the close spacing and higher height above the ground plane.

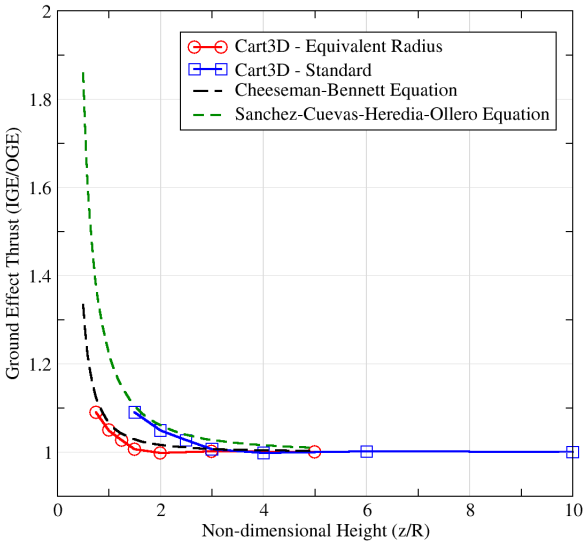

Figure 6. Quad propeller ($s_d = 1.036$) thrust in ground effect at various heights plotted as actual geometric height ("standard") and scaled to an equivalent-area radius. The equivalent-area scaling is a reasonable ground effect model for this configuration as shown by the Cheeseman-Bennett equation.

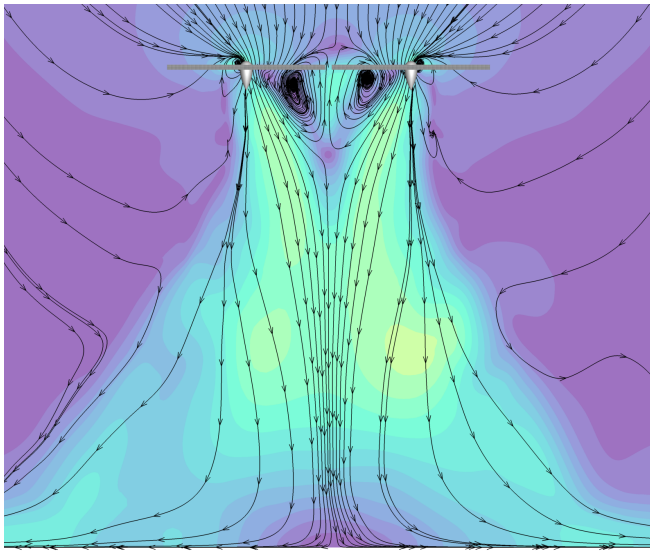

Figure 7. Velocity magnitude (yellow=high, blue=low) with surface streamlines on $y = 0$ cutting plane, showing flow recirculation a significant distance above the ground ($z/R_{eq} = 3$). Rotor hexes are shown in gray and axisymmetric centerbodies in light gray.

AIRBORNE SENSOR PLACEMENT INVESTIGATIONS

This section focuses on developing a methodology towards airborne sensor placement guidelines having established confidence in the present model for simulating multicopter hover aerodynamics in and out of ground effect. There are several steps required to develop any sort of sensor placement guideline. First, a metric must be established to compare the quality of different sensor locations. Next, some assessment of the generalizability of the guideline is needed. If CFD simulations of the exact multicopter geometry and its operating conditions are required, then the benefits of any such guideline will be severely limited. Such detailed simulations

would significantly extend the design cycle as they incur significant computational expense and require design parameters and models that are typically only available when the design is nearly complete.

Flow-field Metric

The goal of optimizing airborne sensor placement is to minimize the impact of the vehicle on the desired measurements. In some cases such as leak detection, this is not as critical because the localization requirements are not as stringent. However, in other cases, the user may be interested in sampling a large area or volume in order to determine the contours of the measured quantity in that region, so any flow mixing could contaminate these types of readings. One approach to assess this effect is to monitor unsteady streaklines to determine all regions of flow that pass through the propellers and see if that flow also enters the sensor(s). Or one could use a similar method of tracking the flow pathlines upstream to determine the original location of fluid parcels that are sampled by the sensor. However, this type of analysis (computationally or experimentally) would be relatively costly and specific to both the aircraft and mission parameters such as the atmospheric conditions and planned flight path. The goal of this work is to determine if more general guidelines for sensor placement can be established without requiring a nearly complete aircraft design. This process could accelerate the design cycle by providing better initial sensor locations and more rapid turnaround for assessing each design if sensor placement is mission critical.

This work focuses on developing guidelines using steady-state CFD simulations, which are a reasonable starting point and typically at least an order of magnitude faster than time-accurate simulations. One possible metric is the stagnation pressure field, because regions with increased p_0 have experienced work done by the propellers. However, this metric will only be valid in regions downstream of the propeller, but it is conceivable that the propeller inflow could affect measurements as well, especially for sensors mounted above the propeller plane. Figures 8 & 9 depict stagnation pressure and velocity magnitude contours around a DJI Phantom 3 hovering out of ground effect (7000 RPM). The contours are very similar, except it is obvious that the stagnation pressure field does not reflect any upstream flow perturbations, as expected, unlike the velocity magnitude contours which reflect the acceleration of the flow into and through the plane of the propellers. While velocity changes are not solely caused by the propeller wakes, they can provide a reasonable metric for easily delineating regions of flow affected by the air vehicle.

Metric Sensitivity and Generalization

In order to further develop the sensor placement guidelines, the sensitivity of the velocity magnitude metric to configuration changes must be assessed. If the sensor accuracy at a given location is strongly influenced by minor design details, such as the exact surface geometry or propeller RPM,

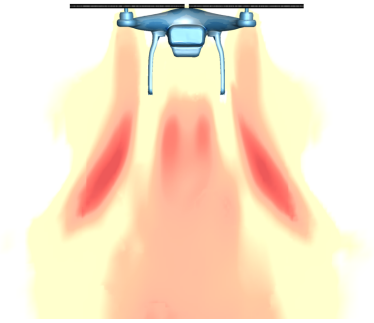

Figure 8. Stagnation pressure contours on a cutting plane through the centerline of a DJI Phantom 3 quadcopter in hover

Figure 9. Velocity magnitude contours on a cutting plane through the centerline of a DJI Phantom 3 quadcopter in hover

it is unlikely that any guidelines will work in general, and their benefit would be strongly reduced. This section investigates several aspects of multicopter design in order to evaluate the generalizability of any proposed velocity magnitude-based criterion for sensor placement.

Airframe First, the sensitivity of the near-body velocity field to small changes in the aircraft configuration is investigated. An approximation to the laser-scanned geometry is developed entirely from intersected geometric primitives. A full description of the approximate geometry can be found in the Appendix, as well as a visual comparison of the two geometries in Figure 22.

The simplified geometry is a moderately faithful representation of the true aircraft that can be quickly generated in any 3-D modeler. Figure 10 compares the velocity magnitude perturbations on a cutting plane through the propeller hub centers due to the differences in fuselage geometry. The quadcopter is in hovering flight two propeller diameters above the ground. Minimal differences are seen in the wake structure in these figures, suggesting that general guidelines may be feasible without requiring a complete, detailed model of the aircraft fuselage.

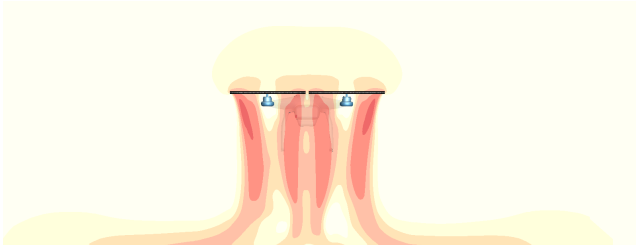

Representative fuselage

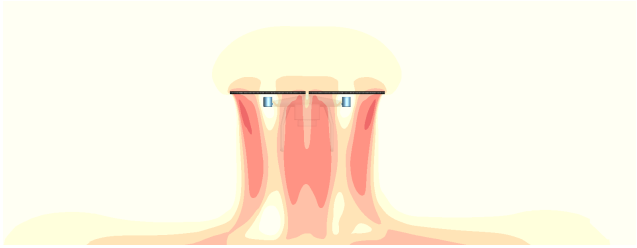

Simplified fuselage

Figure 10. Velocity magnitude contours on cutting plane through forward propeller hubs of DJI Phantom 3 hovering two propeller diameters above the ground showing minor differences between representative fuselage (top) and simplified fuselage (bottom)

Airfoils Multicopter propellers are often provided off-the-shelf with little information about their design or geometry, making them difficult to model accurately in CFD. For this reason, the airfoil performance tables based on the stock DJI propeller are replaced with tables for the Straight-Up Imaging (SUI) Endurance propeller, while the propeller planform is kept unchanged. Figure 11 shows a comparison of the drag polars for the airfoil section at $r/R = 0.75$ operating at a Mach number of 0.16. The actual SUI propeller is 50% larger and operates at a higher chord Reynolds number, so there are fairly significant differences in the polars. The complete details for

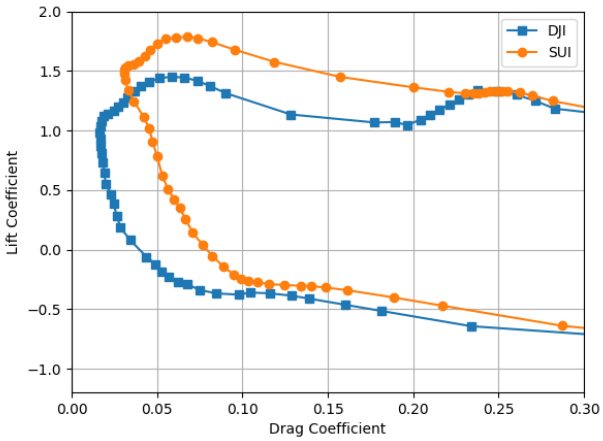

Figure 11. Comparison of the DJI and SUI drag polars for $M = 0.16$ for the $r/R = 0.75$ airfoil sections

the propeller geometry and airfoil sections can be found in the NASA Multicopter Test Report (Ref. 13), but this work focuses on how changes in the airfoil sections affect the velocity field near the aircraft. The velocity magnitude contours in Figure 12 illustrate how this substitution of the airfoil tables results in small changes to the wake structure. Weaker velocity gradients are found in the case with SUI replacement airfoils. However, in terms of sensor placement, the wake trajectory is nearly identical and suggests that the optimal sensor placement will not be too sensitive to the precise specification of the propeller.

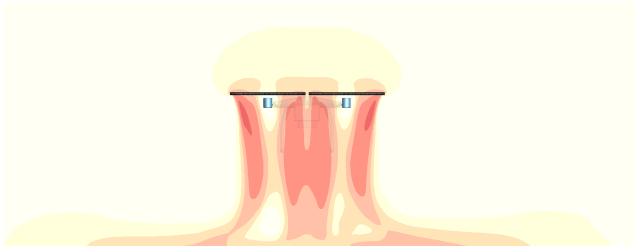

DJI airfoils

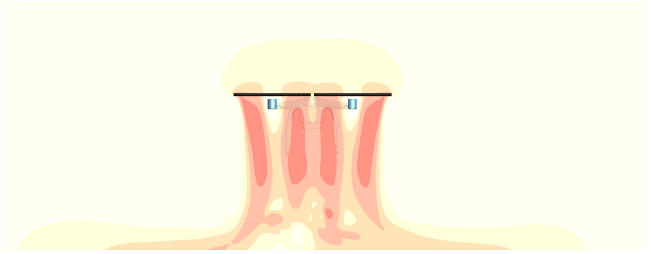

SUI airfoils

Figure 12. Velocity magnitude contours on cutting plane through forward hubs of simplified DJI Phantom 3 hovering two propeller diameters above the ground comparing DJI (top) and SUI (bottom) airfoil performance tables

Aircraft Trim Hovering flight provides basic insight into the problem at hand, but in fact, airborne sensor platforms are frequently operated in forward flight. The (near) geometric symmetry of the hover case simplifies the problem of aircraft trim but is not valid for edgewise rotor-borne flight. Thai et al. (Ref. 24) developed a loosely-coupled trim approach for multi-rotor aircraft and published trimmed body angles and propeller rotational speeds for the DJI Phantom 3 across the flight envelope. Recalling that the goal of the present work is to investigate the feasibility of general guidelines for sensor placement, it is important to assess the impact of aircraft trim. If full trim of the aircraft is required, then any proposed guidelines will not be likely to have broad applicability.

The details of the forward flight simulations are described in the forward flight section below, while this section simply focuses on the difference between trimmed and untrimmed solutions. One case is run with the fully trimmed RPM values from Thai et al. while the second uses a constant RPM for all rotors, which is taken to be the arithmetic mean (4472 RPM) of the four propeller speeds from the fully trimmed case to approximately maintain thrust. The freestream velocity is 15 m/sec (49 ft/sec) and the body pitch angle was $-22.6°$. Although the first case is not perfectly trimmed due to differences in modeling (e.g., fully resolved propellers vs. blade el-

ement source term model), its pitching moment coefficient is nearly two orders of magnitude smaller than the second case. Aerodynamic interactions cause the aft propellers to produce

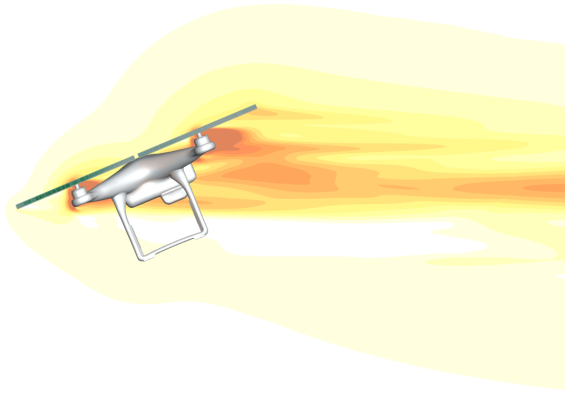

Trimmed RPM

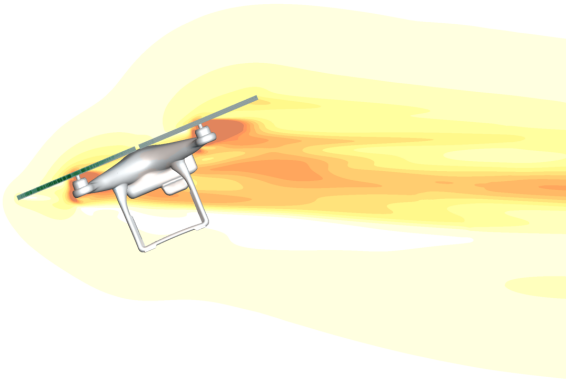

Uniform RPM

Figure 13. Contours of velocity perturbation magnitude on a cutting plane through the centerline of a DJI Phantom 3 quadcopter in edgewise forward flight at 15 m/s demonstrating the effects of aircraft trim on the aerodynamic wakes

less thrust that the forward ones, but the differences in the velocity magnitude field between the two cases is fairly small (Figure 13). Unlike the hover case which had zero far-field velocity, the forward flight plots depict contours of velocity magnitude perturbation, where the freestream velocity has been subtracted out.

Edgewise Forward Flight

As mentioned above, hovering flight provides basic insight into the problem at hand, but edgewise forward flight is a common flight condition that must be considered. The methodology employed in this work was presented previously (Ref. 11), but a short summary is included here for convenience. Note that the previous study (Ref. 11) validated time-accurate simulations, but the results in the present work use the steady rotor model presented earlier for the hover investigations. As in the referenced study, the aircraft was simulated in "free-air" neglecting any wind tunnel wall or installation effects in this work as well.

A computational mesh was generated using the following procedure for each body pitch angle. First, the fuselage (without rotors) was simulated at the specified freestream condition, generating a mesh reasonably adapted (using the method of adjoint-weighted residuals) for accurate force predictions. However, this mesh has no knowledge of propeller-driven off-body flow features and needs finer cells in those wake regions. The trajectory of the propeller wakes is not known in advance, so the grid is iteratively adapted in regions of large velocity gradients. The final mesh, which typically contained around 45 million cells, used an extra buffer layer to smooth out the mesh interfaces. A cutting plane through the mesh at the port rotor hubs is presented in Figure 14, showing the mesh refinement in the steady-state rotor wake. Figure 15 shows a cutting plane through the rotors' plane of rotation with the rotor hexes shown in orange.

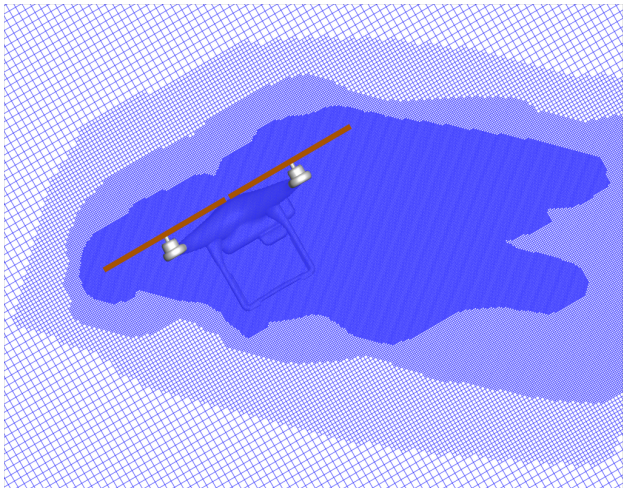

Figure 14. Adapted mesh (blue) on cutting plane through port rotor hub centers with rotor hexes shown in orange for -30° body pitch angle.

Validation Cases

A sweep of simulations is run at various body pitch angles in the range $[-40^\circ, -5^\circ]$ with uniform propeller RPM from 4200 to 6400, corresponding to Table 19 from the experimental dataset (Ref. 13). The goal of this validation exercise is

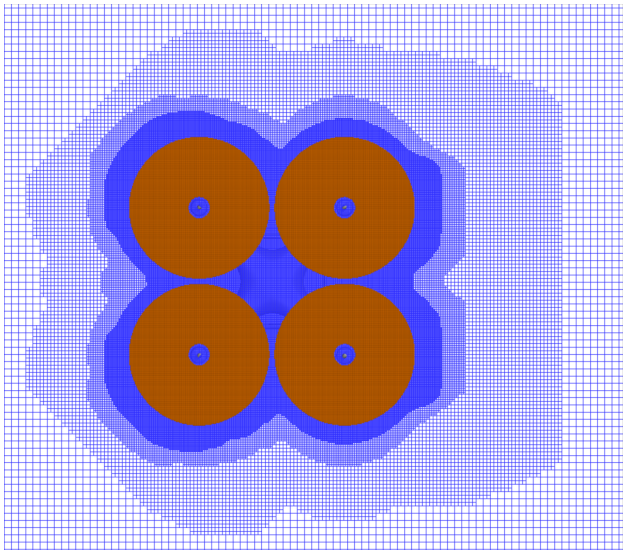

Figure 15. Adapted mesh (blue) on horizontal cutting plane through all rotor hub centers with rotor hexes shown in orange for -30° body pitch angle

v_∞	Pitch (deg)	Propeller RPM
2 m/s (6.6 ft/s)	-1.52	4832
5 m/s (16.4 ft/s)	-2.89	4515
8 m/s (26.2 ft/s)	-4.80	4222
10 m/s (32.8 ft/s)	-13.05	4145
15 m/s (49.2 ft/s)	-22.06	4680

Table 1. Case matrix for DJI Phantom 3 edgewise forward flight simulations

to build confidence in the steady-state model's ability to predict quadcopter forward flight aerodynamics accurately. Figures 16 & 17 clearly demonstrate the accuracy of this present model for edgewise forward flight performance predictions across the range of body pitch angles and propeller speeds. There are some discrepancies at the extremes, which are probably due to the fidelity of the computational model, but overall the agreement is very good for both lift and drag, generally following the experimental trends correctly

Forward Velocity Sweep

This final section leverages the results presented so far and develops a guideline for airborne sensor placement based on simulations of the DJI Phantom 3 in edgewise forward flight. A sweep of forward speeds is performed to assess how the velocity magnitude (perturbation) metric changes with the cruise conditions which are detailed in Table 1.

Figures 18, 19, 20, & 21 illustrate how the velocity field around the aircraft changes with forward speed. As expected, the largest velocity perturbations are found in the rotor wake, which is blown aft quickly at the higher velocities. Several interesting features should be highlighted in these visualizations. First, notice how the propeller streamtube (capture area) increases in size at the lower velocities because of mass conservation. This means that, relative to the vehicle's characteristic length, at slower speeds there is a larger volume of affected air. Comparing Figures 18 & 21 reveals how significant the upstream effects are at low speed. Second, this large capture area and significant flow turning means that a sensor placed above the aircraft will gather samples from different heights depending on its longitudinal position and aircraft speed. For example, at 2 m/s the air going through the aft propellers started more than one propeller diameter above the aircraft, which may be important in certain use cases.

For certain cases, especially at 8 m/s, there appears to be a large region of flow with nearly zero velocity magnitude perturbation. Given its location just above the propellers, it is possible that there are cancelling effects which result in a near-zero perturbation contour, despite it being a potentially poor sensor location.

These validation data and specific forward flight investigations presented in this section make it possible to suggest some preliminary guidelines for sensor placement. As intuition would suggest, below or aft of the aircraft is a poor location because of the fuselage and propeller wakes. At low speeds, a significant amount of air above the aircraft is drawn through the propellers, which introduces uncertainty into the precise sampling location. However, concentration measurements should be fairly accurate if fluid parcels aren't strongly compressed or expanded. There is some upturning of flow ahead of the aircraft as it is entrained into the propeller wakes, but that effect is weaker than the change of direction above the fuselage. In contrast, at higher speeds, locations above or forward of the aircraft outside a 1 vehicle "radius" sphere would seem to be relatively unaffected by the propellers, although perhaps at these speeds one could consider a fixed wing aircraft instead. Of course, there are potential sampling rate and safety issues with flying at high speed, as well as the fact that if multiple passes need to be made, a higher speed pass could be detrimental to future measurements. Finally, there may be some benefit to thoughtful path planning. For example, flying with a headwind could help improve measurements without requiring a faster ground speed.

CONCLUSIONS

This work leveraged a recently developed multi-rotor simulation capability that coupled a fast Cartesian grid Euler solver with a blade element, source term propeller model. The first section of this work investigated the ability of the steady-state method to predict ground effect aerodynamics. After demonstrating mesh convergence and accurate predictions of hover performance out of ground effect, excellent results for the ground effect thrust increase of single propeller were presented, closely matching the classical Cheeseman-Bennett curve. Twin propellers at a close spacing behaved very similarly to the single propeller case. In contrast, the four propeller case showed thrust augmentation at higher heights ($z/R \geq 2$) due to the fountain flow between the propellers. Suggestions in the literature for scaling the radius used in the Cheeseman-Bennett relation using an equivalent total area seem to be invalid for twin propellers but reasonable for the quadruple propeller case, at least for the spacing investigated in this work.

In the second portion of this work, velocity magnitude perturbations were studied in an attempt to create guidelines for airborne sensor placement. Comparison of edgewise forward flight cases with experimental data provided some validation of the modeling approach. Velocity magnitude contours were shown to be a reasonable scalar field to assess flow disturbances due to the aircraft. The wake structure was generally insensitive to the exact propeller airfoils, fuselage shape, and control inputs (trim). Simulations of a DJI Phantom 3 quadcopter in forward flight at low speeds revealed regions of affected air upstream of the vehicle, which reduced in size as forward speed increased. At these higher speeds, the flow is mostly undisturbed outside of 1 characteristic vehicle length both ahead of and above the aircraft. However, at the lower speeds significant flow disturbance is found above the aircraft, whereas the perturbations are more moderate forward of the vehicle.

Author contact:

Jonathan Chiew jonathan.j.chiew@nasa.gov

Michael Aftosmis michael.aftosmis@nasa.gov

Kristen Manies kmanies@usgs.gov

APPENDIX

The approximate DJI Phantom 3 geometry is based off of the laser-scanned geometry from NASA's multicopter test (Ref. 13), but created using only simple geometric primitives. Table 2 lists all of geometric primitives that make up the approximate fuselage geometry. The 3:2 ellipses have their minor axis in the z-direction and are oriented at $\pm 45^\circ$ to the x and y axes. Note that in order to complete the geometry, all of the surfaces need to be mirrored across the $x = 0$ and $y = 0$ planes, except for the rectangular prisms and second linear loft, the latter of which needs to be copied and rotated 3 times in 90° increments around the z-axis.

Element	**Parameters** (mm)
Rect. Prism 1	Corner pts: (-50, -40, -25), (90, 40, 25)
Rect. Prism 2	Corner pts: (15, -30, -45), (60, 30, -25)
Cylinder 1	Axis: (0, 0, 1) at (123, 123, 32)
	Diameter: 14, Height: 30
Cylinder 2	Axis: (0, 0, 1) at (-60, 78, -120)
	Diameter: 5, Height: 120
Rot. Surf. 1	Axis: (0, 1, 0) at (-60, 78, -120)
	Profile: endcap of Cylinder 2, angle: 90°
Lin. Extr. 1	Profile: endcap of Rot. Surf. 1
	Axis: (1,0,0), Length: 60
Linear Loft 1	Sect. 1: Top cap of Cylinder 2
	Sect. 2: Circle (r=10) at (60, 60, 20)
	in z-plane
Linear Loft 2	Sect. 1: Ellipse at (0,0,35), a=30,b=20
	Sect. 2: Ellipse at (118, 118, 25)
	a=12, b=8

Table 2. Geometric primitives for the approximate DJI Phantom 3 quadcopter (in mm)

The comparison images in Figure 22 demonstrate the general similarities between the two fuselage geometries. The approximate fuselage is shown in red, both overlaid and offset from the laser-scanned surface for clarity.

ACKNOWLEDGMENTS

Funding for this work was provided by the USGS National Land Imaging Program and National Innovation Center with partial funding also provided by the NASA Aeronautics Research Mission Directorate's Transformational Tools & Technologies Project. Computer time was provided by the High-End Computing (HEC) Program through the NASA Advanced Supercomputing (NAS) Division at Ames Research Center. The authors would like to thank Carl Russell and Chris Silva of NASA Ames for providing the DJI Phantom 3 geometry.

REFERENCES

1. Brosy, C., Krampf, K., Zeeman, M., Wolf, B., Junkermann, W., Schäfer, K., Emeis, S., and Kunstmann, H., "Simultaneous multicopter-based air sampling and sensing of meteorological variables," *Atmospheric Measurement Techniques*, Vol. 10, (8), 2017, pp. 2773–2784.

2. Gålfalk, M., Nilsson Påledal, S., and Bastviken, D., "Sensitive Drone Mapping of Methane Emissions without the Need for Supplementary Ground-Based Measurements," *ACS Earth and Space Chemistry*, 2021.

3. Gullett, B., Aurell, J., Mitchell, W., and Richardson, J., "Use of an unmanned aircraft system to quantify NOx emissions from a natural gas boiler," *Atmospheric Measurement Techniques*, Vol. 14, (2), 2021, pp. 975–981.

4. Smith, B., John, G., Stark, B., Christensen, L. E., and Chen, Y., "Applicability of unmanned aerial systems for leak detection," 2016 International Conference on Unmanned Aircraft Systems (ICUAS), 2016.

5. Throneberry, G., Hocut, C., and Abdelkefi, A., "Multirotor wake propagation and flow development modeling: A review," *Progress in Aerospace Sciences*, Vol. 127, 2021, pp. 100762.

6. Matus-Vargas, A., Rodriguez-Gomez, G., and Martinez-Carranza, J., "Ground effect on rotorcraft unmanned aerial vehicles: a review," *Intelligent Service Robotics*, Vol. 14, (1), 2021, pp. 99–118.

7. Conyers, S. A., *Empirical evaluation of ground, ceiling, and wall effect for small-scale rotorcraft*, Ph.D. thesis, University of Denver, 2019.

8. Aftosmis, M. J., Berger, M. J., and Adomavicius, G., "A Parallel Multilevel Method for Adaptively Refined Cartesian Grids with Embedded Boundaries," 38th Aerospace Sciences Meeting and Exhibit, AIAA 2000-0808, 2000. DOI: 10.2514/6.2000-808

9. Aftosmis, M. J., Berger, M. J., and Melton, J. E., "Robust and Efficient Cartesian Mesh Generation for Component-Based Geometry," *AIAA Journal*, Vol. 36, (6), 1998, pp. 952–960.

10. Chiew, J. J., *Rapid Computational Aerodynamic Analysis for Multi-Rotor Aircraft*, Ph.D. thesis, Stanford University, 2020.

11. Chiew, J. J., and Aftosmis, M. J., "Integral Velocity Sampling for Unsteady Rotor Models on Cartesian Meshes," AIAA AVIATION 2021 FORUM, AIAA 2021-2624, 2021.

12. Chiew, J. J., and Aftosmis, M. J., "Efficient simulation of multi-rotor vehicles with low Reynolds number propellers," 2018 Applied Aerodynamics Conference, AIAA 2018-4119, 2018.

13. Russell, C. R., Willink, G., Theodore, C., Jung, J., and Glasner, B., "Wind tunnel and hover performance test results for multicopter UAS vehicles," Technical Report TM-2018–219758, NASA, 2018.

14. Tang, E., and Chung, S.-J., "Rapid Extraction of Propeller Geometry Using Photogrammetry," *Bulletin of the American Physical Society*, Vol. 66, 2021.

15. Chiew, J. J., and Aftosmis, M., "A Conservative, Scalable, Space-Time Blade Element Rotor Model for Multi-rotor Vehicles," AHS Aeromechanics Design for Transformative Vertical Flight Conference, 2018.

16. Cheeseman, I., and Bennett, W., "The effect of the ground on a helicopter rotor in forward flight," , 1957.

17. Leishman, G. J., *Principles of helicopter aerodynamics*, Cambridge university press, 2006, pp. 258–259.

18. Del Cont Bernard, D., Giurato, M., Riccardi, F., and Lovera, M., "Ground effect analysis for a quadrotor platform," *Advances in Aerospace Guidance, Navigation and Control*, Springer, 2018, pp. 351–367.

19. Paz, C., Suárez, E., Gil, C., and Vence, J., "Assessment of the methodology for the CFD simulation of the flight of a quadcopter UAV," *Journal of Wind Engineering and Industrial Aerodynamics*, Vol. 218, 2021, pp. 104776. DOI: https://doi.org/10.1016/j.jweia.2021.104776

20. Griffiths, D. A., and Leishman, J. G., "A study of dual-rotor interference and ground effect using a free-vortex wake model," American Helicopter Society 58th Annual Forum, Montreal, Canada, June 11-13, 2002, 2002.

21. He, X., *Modeling and control of in-ground-effect on rotorcraft unmanned aerial vehicles*, Ph.D. thesis, The University of Utah, 2020.

22. Otsuka, H., Kohno, M., and Nagatani, K., "Flow Visualization of Wake of a Quad-copter in Ground Effect," 6th Asian-Australian Rotorcraft Forum and Heli Japan 2017, ARF 2017, 2017.

23. Sanchez-Cuevas, P., Heredia, G., and Ollero, A., "Characterization of the aerodynamic ground effect and its influence in multirotor control," *International Journal of Aerospace Engineering*, Vol. 2017, 2017.

24. Thai, A., Roget, B., Sitaraman, J., and Grace, S., "Multirotor Trim using Loose Aerodynamic Coupling," VFS Aeromechanics for Advanced Vertical Flight Conference, 2020.

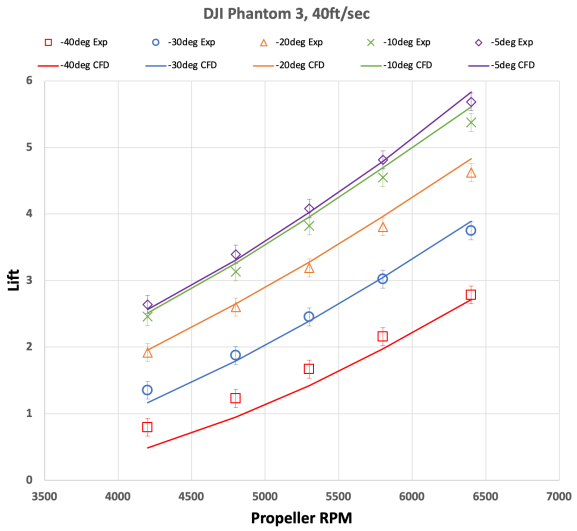

Figure 16. Comparison of lift for DJI Phantom 3 in forward flight with uniform propeller RPM. Experimental data from wind tunnel test at NASA Ames. (Ref. 13)

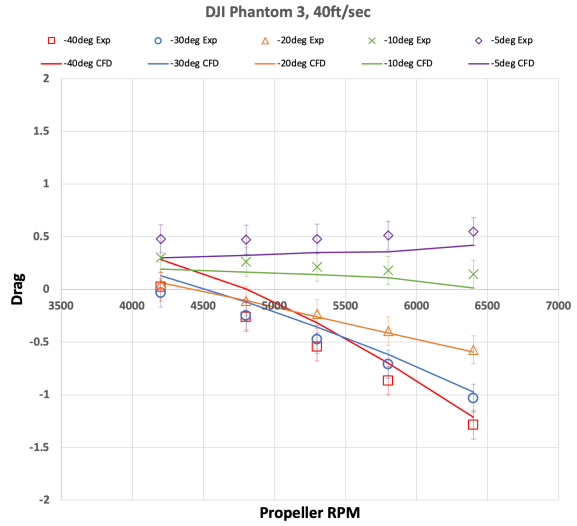

Figure 17. Comparison of drag for DJI Phantom 3 in forward flight with uniform propeller RPM. Experimental data from wind tunnel test at NASA Ames. (Ref. 13)

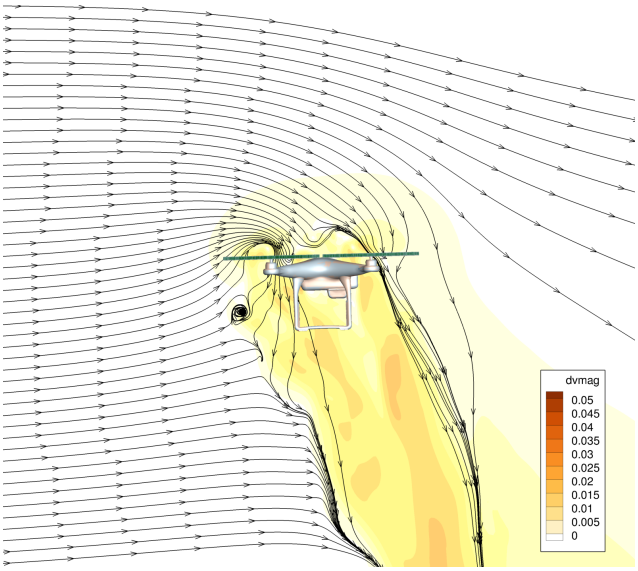

Figure 18. Velocity magnitude perturbations and steady streamlines around a DJI Phantom 3 flying at 2m/s forward velocity, showing significant upstream effects and flow turning.

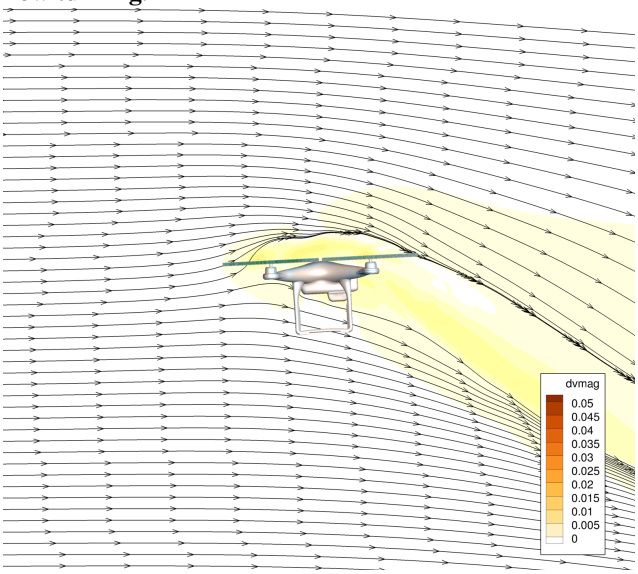

Figure 19. Velocity magnitude perturbations and steady streamlines around a DJI Phantom 3 at 5m/s forward velocity, showing moderate upstream effects and flow turning.

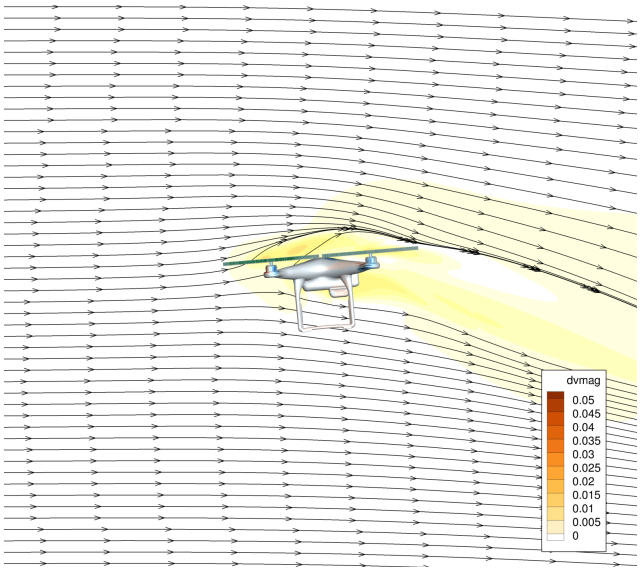

Figure 20. Velocity magnitude perturbations and steady streamlines around a DJI Phantom 3 at 8m/s forward velocity, showing minor upstream effects and flow turning.

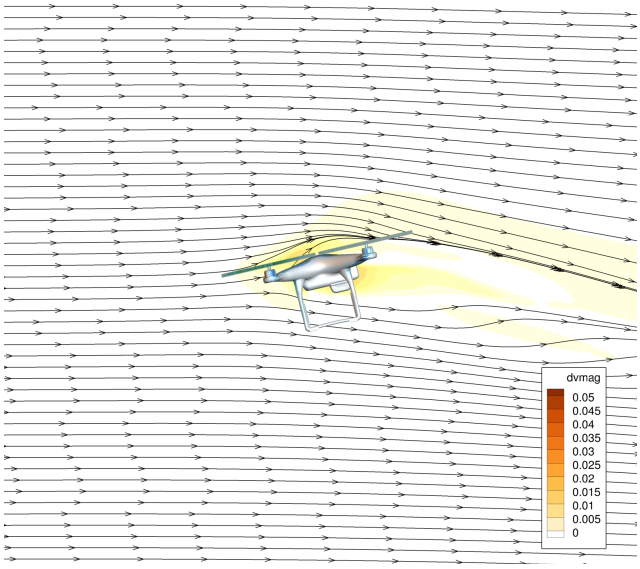

Figure 21. Velocity magnitude perturbations and steady streamlines around a DJI Phantom 3 at 10m/s forward velocity, showing almost negligible upstream effects and flow turning.

Figure 22. Comparison of laser-scanned DJI Phantom 3 geometry (light gray) with approximate fuselage composed of intersected geometric primitives (red). The geometries are presented overlaid (top) and offset (bottom) for clarity.